Regularization-Based 2D Strain Tensor Imaging in Quasi-Static Ultrasound Elastography SAGE Publications

Anne-Lise Duroy, Valérie Detti, Agnès Coulon, Olivier Basset, Elisabeth Brusseau

Regularization-Based 2D Strain Tensor Imaging in Quasi-Static Ultrasound Elastography SAGE Publications

Anne-Lise Duroy, Valérie Detti, Agnès Coulon, Olivier Basset, Elisabeth Brusseau

Regularization-Based 2D Strain Tensor Imaging in Quasi-Static Ultrasound Elastography *SAGE Publications*

Anne-Lise Duroy[1], Valérie Detti[1], Agnès Coulon[2], Olivier Basset[1], and Elisabeth Brusseau[1]

Abstract

Accurately estimating all strain components in quasi-static ultrasound elastography is crucial for the full analysis of biological media. In this study, 2D strain tensor imaging was investigated, focusing on the use of a regularization method to improve strain images. This method enforces the tissue property of (quasi-) incompressibility, while penalizing strong field variations, to smooth the displacement fields and reduce the noise in the strain components. The performance of the method was assessed with numerical simulations, phantoms, and in vivo breast tissues. For all the media examined, the results showed a significant improvement in both lateral displacement and strain, while axial fields were only slightly modified by the regularization. The introduction of penalty terms allowed us to obtain shear strain and rotation elastograms where the patterns around the inclusions/lesions were clearly visible. In phantom cases, the findings were consistent with the results obtained from the modeling of the experiments. Finally, the easier detectability of the inclusions/lesions in the final lateral strain images was associated with higher elastographic contrast-to-noise ratios (CNRs), with values in the range of [0.54–9.57] versus [0.09–0.38] before regularization.

Keywords

Quasi-static ultrasound elastography, regularization, motion tracking, strain tensor

Introduction

Over the past few decades, elastography techniques have been developed for the in vivo investigation of the mechanical properties of biological tissues.[1–4] These techniques have been introduced for diagnostic purposes since significant changes in the mechanical properties are expected between healthy and pathological tissues.[5] Different approaches are available depending on the imaging modality employed, the mechanical stress used and the parameter to be determined. The present study focuses on quasi-static ultrasound elastography, which produces strain images of media subjected to compression.[6] Commonly, only axial strain (along the acoustic beam) is estimated. Nevertheless, axial strain imaging has proved to be a valuable tool for distinguishing regions with different stiffnesses within a medium, and many studies have shown improved diagnostic performances when combining elastography with B-mode imaging, versus B-mode imaging alone.[7–9] Moreover, recent work comparing axial strain and shear-wave ultrasound elastography reported similar performances for the two techniques.[10–12]

As reported by some authors, estimating not only the axial strain but also the full strain tensor could provide useful supplementary information. Konofagou and Ophir,[13] for instance, developed a weighted interpolation-based approach to estimate both axial and lateral strains, which make it possible to deduce the Poisson's ratio distribution within tissues. The time evolution of this strain ratio during sustained compression, also called the

[1]Univ Lyon, INSA-Lyon, Université Claude Bernard Lyon 1, UJM Saint-Etienne, CNRS, Inserm, CREATIS UMR 5220, U1294, Villeurbanne, France
[2]Département de radiologie, Centre de lutte contre le cancer Léon Bérard, Lyon, France

Corresponding Author:
Elisabeth Brusseau, CREATIS, Bâtiment Léonard de Vinci - 21 Avenue Jean Capelle, Villeurbanne Cedex 69621, France.
Email: elisabeth.brusseau@creatis.insa-lyon.fr

effective Poisson's ratio, is a parameter that is assessed to characterize poroelastic materials in elastography.[14–17] Likewise, information on lesion mobility can be provided by estimating the shear strain components[18–21] or rotation elastograms.[22,23] Bonding information could be helpful for distinguishing benign from malignant lesions when stiffness alone remains insufficient, since benign lesions tend to be loosely bonded, whereas malignant ones are more firmly bonded to the surrounding tissues. This more or less mobility of lesions should result in different shear strain features. Finally, accurately estimating all strain components is essential for a full analysis of a medium, not only through a more complete visualization of the tissue response, but also through implementation of further computational methods necessary to solve the inverse problem.[24–26]

Determining the strain tensor requires computation of the displacements. Numerous methods are described in the literature for estimating the different components of tissue displacements.[13,27–34] Nonetheless, radiofrequency (RF) ultrasound images are characterized by anisotropic resolution, which leads to coarser-quality fields for the displacement components orthogonal to the axial direction. This results in strain images highly affected by noise. Different methods have been introduced to improve displacement estimation, especially of lateral displacement. Some developments place more focus on the data used. For instance, in the work by Techavipoo et al.[35] and Xu and Varghese,[36] displacement is determined from estimations made along multiple insonification angles. Selladurai and Thittai[37] introduced a specific ultrasound probe, in which the array of transducers can move to sub-pitch locations thanks to an integrated motor. Acquiring additional RF signals at sub-pitch positions was shown to produce results—in this work, rotation elastograms—with higher contrast-to-noise ratios (CNRs) than those from conventional imaging. Specific RF images more adapted to tracking the lateral displacement of tissues were also described in.[38,39] These RF images include lateral oscillations, resulting from a particular beamforming. As an alternative to the use of specific data sets, some other approaches focus more on the strain estimation method itself to reduce noise in elastograms, involving notably modified block-matching and/or regularization techniques.[13,40–44] This can involve the use of a supplementary condition to constrain the estimated displacements, such as the tissue incompressibility[45–47] or the equilibrium conditions.[40] Enforcing one of these conditions results in smoothing of the displacement fields. Guo et al.[41] recently proposed an approach referred to as "partial differential equation (PDE)-based regularization method", which uses the (quasi-) incompressibility property of soft tissues. This method has shown promising results, with a significant increase in the CNR for the lateral strain component in particular. However, with such an approach, some images, especially shear strain ones, are affected by line artifacts, which corrupt the strain patterns as shown in Duroy et al.[48] and in some results of this article.

In this study, we investigated two-dimensional (2D) strain tensor imaging, and more particularly the improvement in strain images resulting from the introduction of a specific regularization method. This method enforces the property of tissue (quasi-) incompressibility while penalizing strong field variations, and is applied to the displacement fields estimated using a motion-tracking technique we previously developed for elastography purposes.[49] The strain images are then computed from the gradient of the estimated displacements. The article is organized as follows: A detailed description of the regularization method developed is provided in the next section, along with the material used for assessing its contribution in strain imaging. Results obtained with data from numerical simulations, phantom experiments and patient examinations are then presented and discussed. In particular, an assessment of the method, when applied to experimental data, will be conducted with the computation of CNR values. Finally, in the last section, we present the conclusions of this study.

Materials and Methods

Method

This first section presents the overall method developed for 2D strain tensor imaging. It comprises two main steps: an initial estimation of the displacement fields, then their regularization. Images of all the strain components are finally computed from the gradient of the displacements.

Step 1: Estimation of the displacement fields. As mentioned earlier, a large variety of approaches can be employed to estimate compression-induced internal displacements of tissues from RF ultrasound images. The method developed by our group and used in this study is briefly explained here. We refer the reader to the following papers for additional information.[28,49]

The basic principle of the method is the following: let us consider two RF images, I_1 and I_2, acquired during medium deformation. The first image I_1 is subdivided into multiple 2D regions of interest (ROIs) of the same dimensions, regularly positioned and overlapping each other. For each one of these ROIs, the deformed replica in I_2 is identified via the maximization of a similarity criterion chosen as the correlation coefficient (*CC*). Contrary to most motion-tracking methods, where only a 2D shift is considered, an axial scaling factor α is also used to describe the ROI transformation between I_1 and

I_2. This factor allows us to take into account the shape variations that occur in the RF signal due to the medium deformation.[50–52] Along the lateral direction, however, scaling is ignored because of the coarser image resolution. Note that the correlation coefficient provides an indication of the match achieved during parameter estimation: The closer the value to 1, the better is the match. Several situations can lead to correlation coefficient values much less than 1 at the solution, such as errors in the parameter estimation or ROI variations between images too complex to be described well by the model used. In the case of an insufficient match, defined as a CC lower than a threshold Th, the estimates are labeled as untrustworthy, and a local regularization is applied to ensure continuity with spatially close estimates characterized by $CC \geqslant Th$. The threshold Th is set at 0.75, value found to be adapted for the analysis of biological tissues. It was determined empirically during our previous work.

During elastography experiments, sequences of RF images are typically acquired. With our method, parameters are calculated between consecutive RF images, in order to limit errors due to out-of-plane motion. Indeed such motion is expected to be lower between two successive frames than between the first and the last frame of the sequence considered. The final displacement fields are then obtained by combining the contribution of the different pairs of images. As will be illustrated in the Results section, this method enables one to accurately estimate the axial displacement field but the lateral one remains generally too noisy to be used directly for strain computation.

Step 2: Regularization. The second step of the proposed method consists in regularizing the previously estimated displacements using the (quasi-) incompressibility property of tissues. Contrary to the regularization method mentioned in step 1, whose application is local, the one here is performed unconditionally over the whole image.

Let $\bar{\boldsymbol{d}}$ be a displacement previously estimated in a domain Ω, whose axial and lateral components are $\bar{u}_y$ and $\bar{u}_x$, respectively. Regularized displacements u_y and u_x are obtained by solving the following optimization problem:

$$\underset{u_x,\, u_y}{Minimize} \quad F(u_x, u_y)$$

with:

$$\begin{aligned} F(u_x,u_y) = & \int_\Omega \left(\frac{\partial u_y}{\partial y} + \frac{\partial u_x}{\partial x}\right)^2 + \lambda_1 \int_\Omega (u_y - \bar{u}_y)^2 \\ & + \lambda_2 \int_\Omega (u_x - \bar{u}_x)^2 + \beta_1 \int_\Omega \left(\left(\frac{\partial u_y}{\partial x}\right)^2 + \left(\frac{\partial u_y}{\partial y}\right)^2\right) \\ & + \beta_2 \int_\Omega \left(\left(\frac{\partial u_x}{\partial x}\right)^2 + \left(\frac{\partial u_x}{\partial y}\right)^2\right) \end{aligned} \tag{1}$$

where λ_1, λ_2, β_1, and β_2 are the weighting coefficients. The first term in F is related to the incompressibility condition, while the following two are the data fidelity terms, and the last two are penalty terms. λ_1, λ_2, β_1, and β_2, which are all constant and positive, modulate the regularization weight on the fields. As in Guo et al.,[41] the property of (quasi-) incompressibility of tissues is used for regularizing the displacements fields. However, compared with their approach, F comprises two additional terms that penalize strong spatial variations within the axial and lateral displacement fields. These terms were added in order to reduce some artifacts observed in the shear strain images. Indeed, when first using this approach without the penalty terms, that is, with $\beta_1 = \beta_2 = 0$, and with our motion-tracking technique, we noted that the lateral displacement fields appeared relatively smooth along the lateral direction, but with some small variations along the axial direction, leading to a slight effect of "horizontal lines" in the corresponding images.[48] These lines do not affect the lateral strain fields but largely degrade the shear strain ones.

To solve the optimization problem described in (1), Euler-Lagrange equations are introduced. Indeed, the axial and lateral displacements that minimize F, will also satisfy the Euler-Lagrange equations. With our problem, these equations write:

$$\begin{cases} \lambda_1(u_y - \bar{u}_y) - (1+\beta_1)\frac{\partial^2 u_y}{\partial y^2} - \frac{\partial^2 u_x}{\partial x \partial y} - \beta_1 \frac{\partial^2 u_y}{\partial x^2} = 0 \\ \lambda_2(u_x - \bar{u}_x) - (1+\beta_2)\frac{\partial^2 u_x}{\partial x^2} - \frac{\partial^2 u_y}{\partial x \partial y} - \beta_2 \frac{\partial^2 u_x}{\partial y^2} = 0 \end{cases} \tag{2}$$

Determining u_y and u_x is performed by using the gradient descent method, in which the gradient term is given by the left-hand side of equation 2. Displacement derivatives are approximated using finite differences and the Neumann boundary condition at $\partial\Omega$, $\nabla \boldsymbol{d}\boldsymbol{n} = \boldsymbol{0}$, with $\boldsymbol{n}$ the outward normal at the boundary. The step size used in the gradient descent is constant and equal to $\frac{\delta x^2 \delta y^2}{4(\delta x^2 + \delta y^2)}$, where δx and δy are the lateral and axial size of the pixels in the displacement images to be regularized.

Concerning the weighting coefficients λ_1, λ_2, β_1, and β_2, they are tuned by visual inspection of the results, such as to improve them in terms of noise reduction and inclusion/lesion detectability. Lastly, two criteria are used to stop the iterative process. The 1^{st} stopping criterion is chosen as:

$$\sqrt{\sum_{pixels} ((u_y^k - u_y^{k-1})^2 + (u_x^k - u_x^{k-1})^2)} < \xi \tag{3}$$

also written $C_{rite} < \xi$, with u_y^k and u_x^k the displacement fields at iteration k, and $\xi = 10^{-8}$, considering that the results remain quasi-unchanged below this threshold. The 2^{nd} stopping criterion is chosen as a maximum number of iterations allowed N, here $N = 50,000$. The fields

are thus iteratively updated until one of the two stopping criteria is reached.

Materials and Data Acquisition

In this study, a first evaluation of the method is carried out using data of increasing complexity, from numerical simulations to in vivo tissue images. With the simulations, the actual displacements and strains are known and allow the accuracy of the developed method to be assessed, whereas the experimental data are used to determine whether the method is still able to perform strain tensor imaging in more complex cases (phantoms, breast tissues). The tests with phantoms are an intermediate step for method assessment, as these objects are less complex than biological tissues. Moreover, for those examined in this work, mechanical information is given by the manufacturer, which will help us analyze the experimental strain fields. For in vivo breast tissues, no such information is available, preventing, for instance, any analysis about the strain ranges or specific strain patterns from being performed. However, they reveal the complexity of breast elastography, for which our method is developed.

The different media used in this work are described below, along with the chosen evaluation criteria.

Numerical simulation description. Initial tests were conducted with numerical simulations. A $60 \times 40 \times 40\text{-}mm^3$ linear, elastic, isotropic, and homogeneous medium with a Young's modulus of 10 kPa and Poisson's ratio of 0.49 was simulated using *Comsol Multiphysics*®. In this simulation, the medium was subjected to uniaxial loading, resulting in uniform strain of the material. Ten compression levels were considered, from 1% to 10%, in steps of 1% axial strain. These values are in the range of strains typically observed in quasi-static ultrasound elastography. Since a 2D method was developed in this study, we retained for each compression level, the axial and lateral displacement of the median plane. Radiofrequency ultrasound images were then generated as follows. The initial medium was modeled as a collection of ultrasound scatterers, with a spatially uniform distribution, and with amplitudes normally distributed, and the corresponding RF image was produced by convolution of the set of scatterers with the point spread function (PSF) characterizing the ultrasound system. In order to use a realistic PSF, the one of our *Ultrasonix* ultrasound scanner (Ultrasonix Medical Corporation, Richmond, BC, Canada) was measured experimentally, by imaging the cross-section of a 20-μm in diameter tungsten wire. The probe used was the L14-5W/60, the selected frequency on the scanner 6.6 MHz, and the sampling frequency 40 MHz. Finally, for each compression level, scatterers were moved according to the displacements provided by *Comsol Multiphysics*® and the ultrasound images generated exactly as described above, resulting in a 11-frame sequence of the medium under increasing deformation. It should be noted that displacement estimation from these simulations was performed as with experimental data, that is, initial displacement fields were computed from the consecutive RF image pairs and the results combined to yield the evolution of these fields, relative to the first image of the sequence. Regularization was then applied to the displacement fields obtained for each compression level.

Experimental data acquisition. The method was also assessed with experiments on three *CIRS* (Computerized Imaging Reference Systems, Norfolk, VA, USA) phantoms: two breast elastography phantoms (models 059) and one elasticity QA phantom (model 049). The *CIRS* models 059 mimic a female breast in the supine position, within which several spherical inclusions are embedded. The Young's modulus of these inclusions is approximately three times that of the background. Here, two regions were scanned, one containing a single inclusion (case #1, Figure 1(a)), and the other two inclusions one above the other (case #2, Figure 1(b)). The *CIRS* model 049 is a parallelepiped-shaped medium inside which there are several spherical inclusions of different stiffnesses. Data were acquired from a region consisting of a 10 mm in diameter inclusion of Young's modulus of 47 kPa, and positioned in a 26.5 kPa background (case #3, Figure 1(c)). It should be indicated that the phantom specifications are all provided by the manufacturer.

For each region examined, a typical quasi-static elastography experiment was performed, that is, the medium was cautiously and continuously compressed and decompressed by the operator using the ultrasound probe while the RF images were acquired. Data were collected with an *Ultrasonix* ultrasound scanner equipped with an L14-5W/60 transducer. The sampling frequency was 40 MHz.

Finally, the method was also assessed with in vivo data collected during patient examinations (case #4, Figure 1(d); case #5, Figure 1(e); case #6, Figure 1(f)). More precisely, these data were extracted from an archived database, resulting from a previous breast elastography study. Detailed information on this study can be found in the article by Brusseau et al.[49]. It should be underlined that the data acquisition for in vivo tissues was conducted similarly to that for the phantoms. The cases selected are two of an invasive ductal carcinoma (IDC) (cases #4 and #5) and one of a fibroadenoma (case #6).

Results are presented in the remainder of the article, with displacement and strain fields obtained during medium compression (cases #1, #3, #4, #5, and #6) and decompression (case #2), for a more complete illustration.

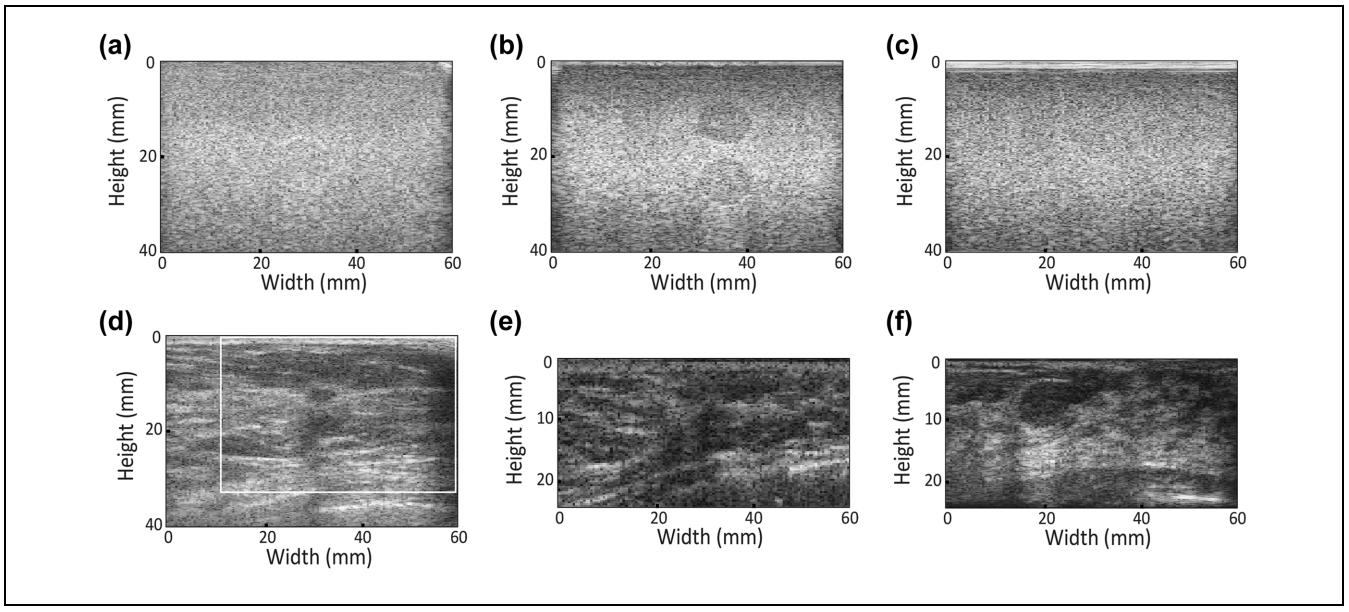

Figure 1. B-mode images from, (a-c) phantom cases #1, #2, and #3, and (d-f) in vivo breast tissue cases #4, #5, and #6. In case #4, displacement estimation was performed in a preselected area (white box).

Assessment Criteria

The evaluation of the results is based on different criteria, depending on the type of the data analyzed. For numerical simulations where the actual values were known, the mean and standard deviation of estimated strains obtained for each compression level were computed and compared with the theoretical values. This was performed for axial, lateral, and shear strains, before and after regularization.

Then, for the phantom cases for which actual strain values are inaccessible, experiment modeling was performed to obtain strain images with which the estimated ones can be compared. Each numerical model was built with *Comsol Multiphysics*®, using the information provided by the manufacturer. Simulated media consisted of a 3D parallelepiped-shaped homogeneous background containing spherical inclusion(s), the different regions being made of a linear elastic and isotropic material. The simulations reproduced the configuration of media deformed using a transducer, which results in only part of the medium top surface being subjected to displacement. The applied displacement was considered to be vertical and was manually adjusted to obtain values similar to those measured experimentally. The bottom surfaces of the media were prevented from moving in the axial and elevational directions, whereas their vertical surfaces were let free to move. These boundary conditions allowed us to get closer to the experimental results. Although modeling the experiments perfectly is not possible, these simulations provide elements with which the experimental results can be compared, such as the range of lateral strain values or shear strain patterns. This should help us to assess and analyze the experimental fields.

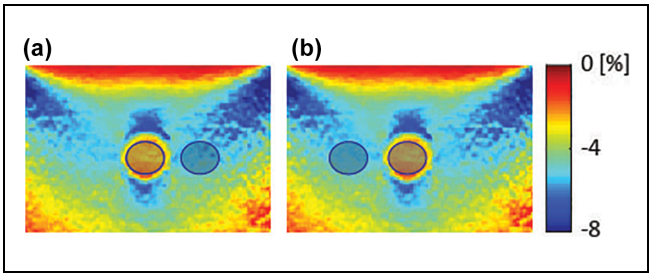

Figure 2. Illustration of the region selection for CNR computation with the axial strain image from phantom case #1. For the region selected in the background, two different positions are considered, (a) on the right and (b) on the left of the inclusion.

To provide a more quantitative assessment of the performance of the proposed method, contrast-to-noise ratios were also computed. The CNR is widely employed in elastography studies as an indicator of lesion detectability within an image. It is computed as follows:

$$CNR = \sqrt{\frac{2(\bar{s}_i - \bar{s}_b)^2}{\sigma_i^2 + \sigma_b^2}} \tag{4}$$

where $\bar{s}$ and σ denote the mean and the standard deviation of the strain, respectively, within a region inside the inclusion (subscript i) and the background (subscript b). These regions are selected using two circular ROIs of identical size and positioned at the same depth. For each inclusion, two CNRs are computed, one by selecting the

background region on the right of the inclusion (Figure 2(a)) and the other one on the left (Figure 2(b)). The multiplying factor (MF) is also calculated as the ratio of CNRs after and before the regularization.

Finally, for the in vivo cases, only the CNR was computed, as no mechanical information about the examined tissues is available.

Results

Before detailing the results, some comments on the choice of the weighting coefficients should be made. First, these coefficients were tuned manually by visual inspection of the results in order to improve them in terms of noise reduction and inclusion/lesion detection. It is interesting to note that the values of λ_1, λ_2, β_1, and β_2 were kept unchanged in all of the cases examined in this study. For displacement fields in millimeters, the values of λ_1 and λ_2 are 10 and 0.03, respectively. This choice was made for λ_1 to prevent any loss of quality in the axial displacement and strain, and for λ_2 to allow for sufficient modifications in the lateral components. To illustrate their influence on the regularized fields, an example is given with the phantom case #1. First, for both λ_1 and λ_2 (Figure 3), the displacements, and thus the strain fields, are significantly modified when λ is small (e.g., 0.01) but nearly unchanged for larger values (e.g., 10). More specifically, in Figure 3(b), axial displacement fields very similar to the one initially estimated can be observed for the different values of λ_1, except for $\lambda_1 = 0.01$, which shows stronger variations. In addition, these fields, when similar, needed approximately the same number of iterations to be regularized. However, even imperceptible changes in the displacements can strongly impact the strain fields (e.g., $\lambda_1 = 0.1$), and a degradation of the axial strain is noticeable when λ_1 is no longer sufficiently high. On the contrary, the lateral displacement and strain fields are improved for lower values of λ_2 by allowing, to a certain extent, modifications within these fields (Figure 3(c)). For instance, a value of 0.01 leads to a regularized lateral displacement that is different (on the top of the image) from the one initially estimated, and to a shear strain a little bit more corrupted compared with $\lambda_2 = 0.055$. Yet, when λ_2 increases, the lateral strain field become less smooth, which suggests that adapted values of λ_2 can be chosen between 0.01 and 0.055. Thus, with the weights $\lambda_1 = 10$ and $\lambda_2 = 0.03$, the regularization will mostly modify the lateral fields and the regularized displacement fields will remain coherent with the estimated ones.

Concerning β_1 and β_2, different tests were conducted with values ranging from 0 to 0.5. To illustrate the influence of these weighting coefficients, results are given in Figure 4, still using the phantom case #1. Results are shown for β_1 equal to $0, 0.05$, or 0.5 while β_2 is fixed at 0, and conversely. The simulated fields obtained by modeling the experiment with *Comsol Multiphysics*® are also displayed to help in the analysis of the results. As it can be expected, β_1 acting on an already very smooth axial displacement, it has a very limited impact on the regularized fields (e.g., with the axial displacement, the axial strain and the shear strain, Figure 4(a2–a4, c2–c4, d2–d4)). On the contrary, β_2 tends to modify the lateral displacement fields efficiently (Figure 4(b2–b4)), and thus, the lateral strain (Figure 4(e2–e4)). However, for $\beta_2 = 0.5$, the shear strain (Figure 4(d4′)) is less consistent with the simulation (Figure 4(d1)), which suggests a loss of information in the regularized lateral displacement (Figure 4(b4)). Indeed, the contribution of the lateral displacement in the shear strain is significantly reduced, leading to a shear strain dominated by the axial-shear component. If small values of β_2 enhance the regularized fields, a too-strong penalty seems, conversely, to degrade them. For β_1, despite its minor influence in the example provided, it can be selected equal to β_2 to ensure smoothing on potentially degraded axial displacements. Therefore, the choice was made to set both β_1 and β_2 to 0.05. In the following, results obtained with a regularization ignoring the penalty terms ($\beta_1 = \beta_2 = 0$) will also be provided for comparison.

Numerical Simulation Results

The results obtained with the simulated homogeneous medium subjected to 10 different levels of compression are displayed in Figure 5. For each compression level, the mean and standard deviation are computed for the same selected area (white box) for the axial, lateral, and shear strains, before and after regularization. A region of interest was selected because a decrease in the values was observed along the vertical edges of the regularized lateral strain fields; these values were therefore excluded from the analysis. Surprisingly, even though the estimated lateral strain displays only noise before regularization (Figure 5(b), second column), resulting in a large standard deviation, the mean value remains close to the true one, for each compression step. Applying regularization (with or without the penalty terms) lowers these mean values slightly, while drastically decreasing the standard deviations. Likewise, shear strains before regularization present large standard deviations but mean values close to the true ones. After regularization, the standard deviations decrease and the fields appear much less noisy, especially for $\beta_1 = \beta_2 = 0.05$ (Figure 5(c), third column). Finally, concerning the axial strain, similar mean values can be observed between the simulated, estimated, and regularized fields, as well as very low

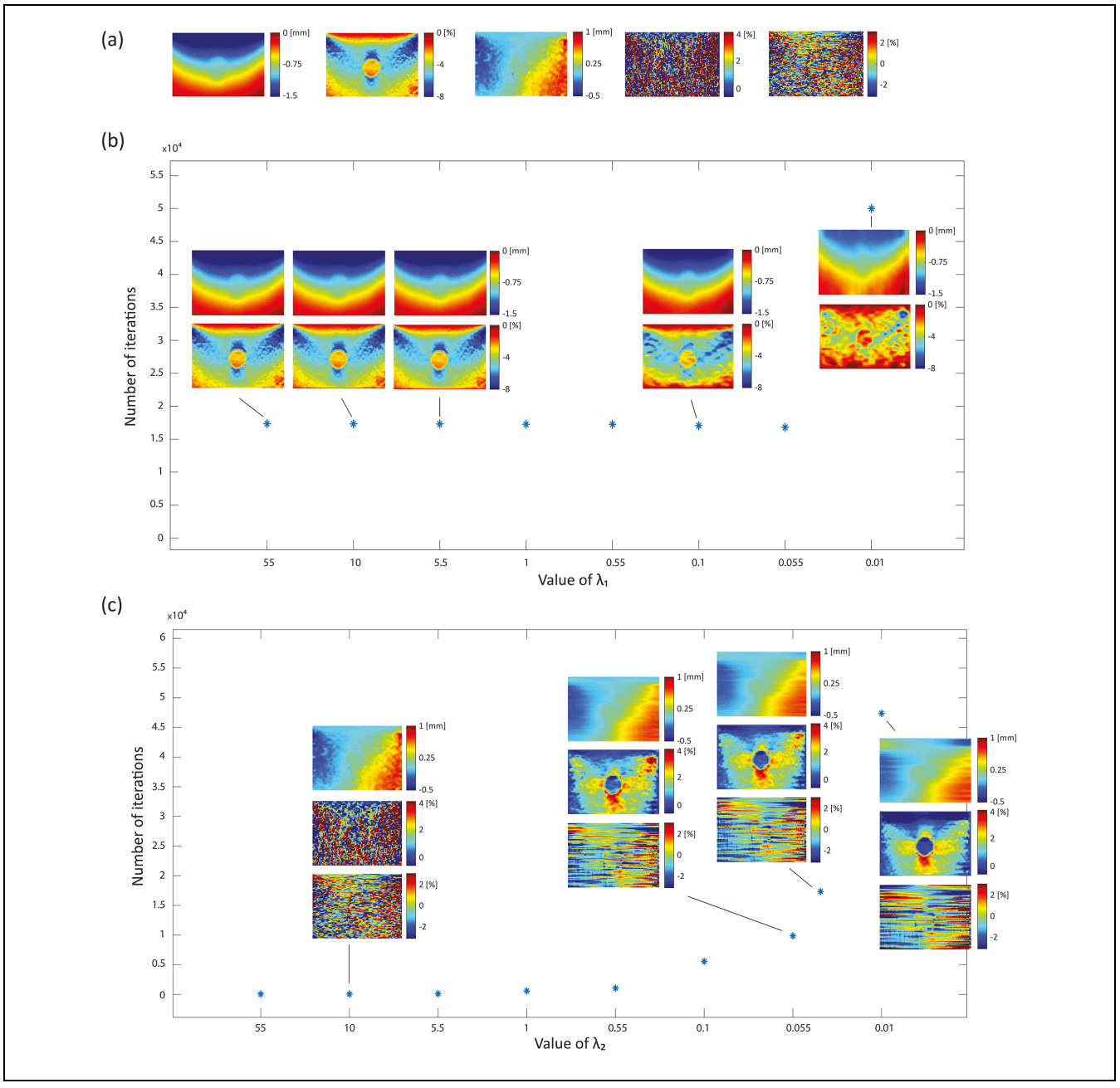

Figure 3. Illustration of the influence of the weighting coefficients λ_1 and λ_2 (when $\beta_1 = \beta_2 = 0$) on the displacement and strain fields, with the phantom case #1. (a) Initial fields, from left to right: axial displacement, axial strain, lateral displacement, lateral strain and shear strain. (b) Regularized axial displacement (top) and axial strain (bottom) for five different values of λ_1, with λ_2 fixed at 0.03, (c) Regularized lateral displacement, lateral strain and shear strain (top to bottom) for four different values of λ_2, with λ_1 fixed at 10. In (b) and (c), the number of iterations at the solution is also represented (*).

standard deviations, whether the regularization method is applied or not. Overall, we can note that the introduction of penalty terms $\beta_1 = \beta_2 = 0.05$ has a limited influence on the mean values of the strain tensor components, but allows a strong decrease of the standard deviations, especially in the shear strain images.

Phantom Results

The results for case #2 and case #3 are displayed in Figures 6 and 7, respectively. Those from case #1 are not given here as images from this case were already shown when analyzing the influence of the weighting coefficients. For these cases, similar comments can be made.

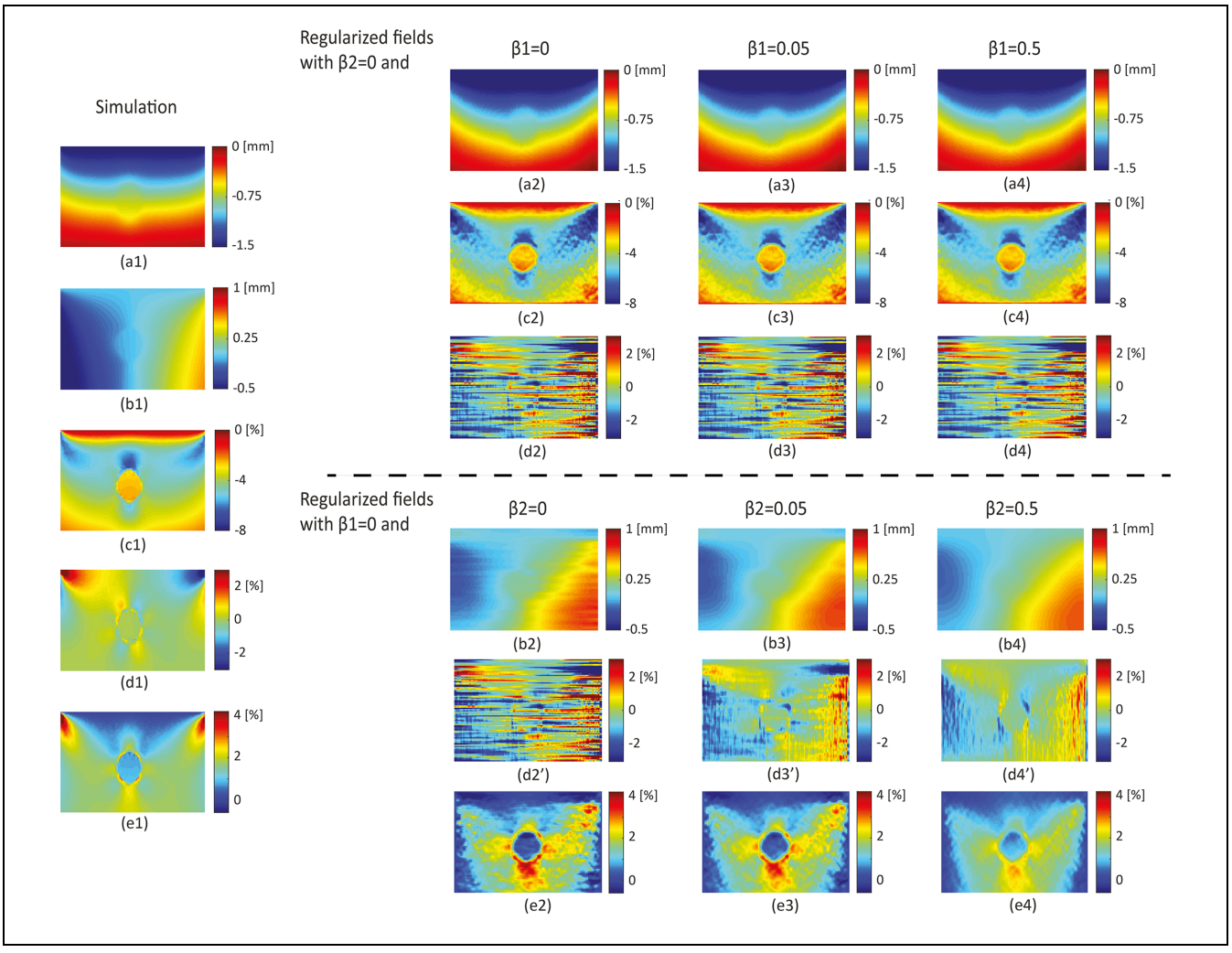

Figure 4. Illustration of the influence of the weighting coefficients β_1 and β_2 (when $\lambda_1 = 10$ and $\lambda_2 = 0.03$), with the phantom case #1. On the right, the regularized displacement and strain fields, and on the left (simulation), fields resulting from the modeling of the experiment with *Comsol Multiphysics*®. From (a) to (e): axial displacement, lateral displacement, axial strain, shear strain, and lateral strain.

Unlike the initial axial displacement (Figures 6 and 7, (a)), the lateral displacement before regularization (Figures 6 and 7, (e)) is noisy, and cannot provide useful information about the phantom lateral strain (Figures 6 and 7, (q)). However, both displacements remain in agreement with the simulated fields (Figures 6 and 7, (d) and (h)). As a reminder, these simulations were built to provide elements of comparison. It should, however, be bear in mind that some differences are expected, since perfectly modeling free-hand elastography experiments cannot be achieved.

After regularization without penalty terms ($\beta_1 = \beta_2 = 0$), the lateral displacement (Figures 6 and 7, (f)) is smoother compared with the initial fields (Figures 6 and 7, (e). This smoothing is sufficient to significantly improve the lateral strain, leading to images where the inclusions are clearly revealed (Figures 6 and 7, (r))). For case #3, the presence of a second inclusion of different stiffness even becomes visible at the left border of the image, although it is partly outside the imaging area. This inclusion is in agreement with the phantom specifications, and corresponds to a 10 mm in diameter sphere of Young's modulus of 13kPa. For these two cases, the lateral strain field (Figures 6 and 7, (r)) is consistent with its corresponding simulated field (Figures 6 and 7, (t), and exhibits the same range of strain values, which was not the case before. Indeed, before regularization, the lateral strain (Figures 6 and 7, (q)) is highly affected by noise, leading to a much wider range of values.

By contrast, the regularization has no visible impact on the axial displacement (Figures 6 and 7, (a) and (b)), and on the axial strain (Figures 6 and 7, (i) and (j)), as expected. Concerning the shear strain (Figures 6 and 7, (n)), the improvement is weaker than for the lateral

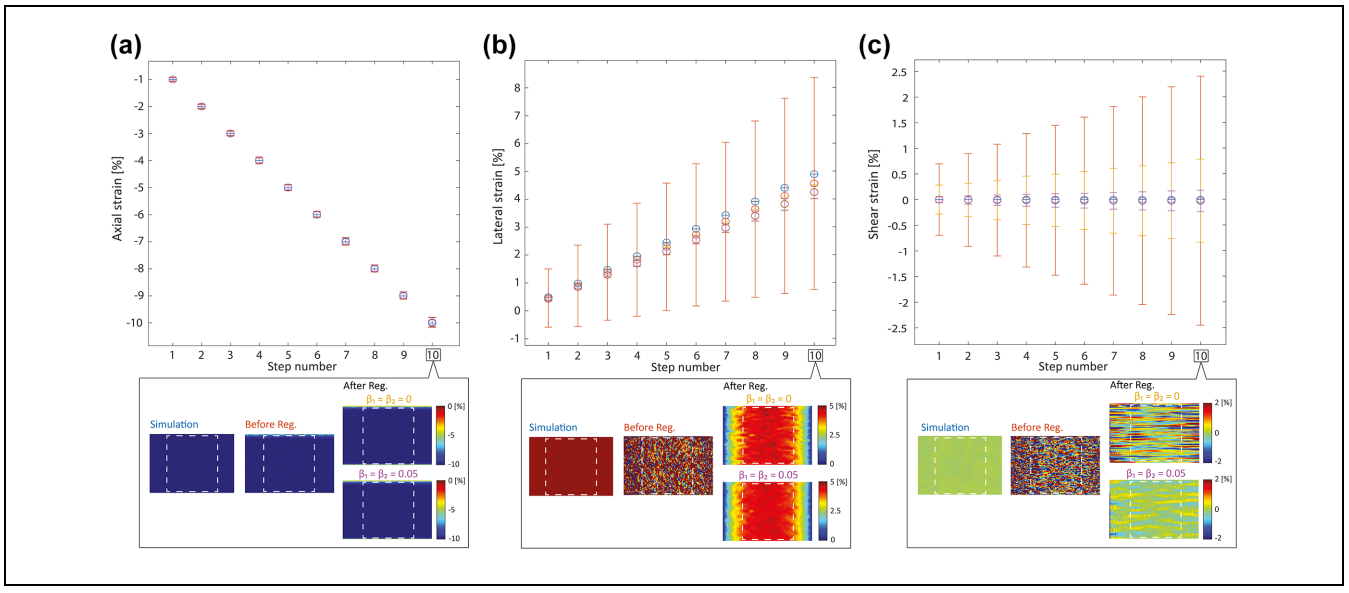

Figure 5. Simulation results obtained for a linear elastic, isotropic, and homogeneous medium subjected to 10 levels of compression. (a) Axial strain, (b) lateral strain, and (c) shear strain. Top: simulated (blue), initially estimated (red), and regularized ($\beta_1 = \beta_2 = 0$(yellow) or $\beta_1 = \beta_2 = 0.05$ (purple)) fields, for axial strains varying from 1% to 10% in steps of 1%. The mean strains and the standard deviations are calculated within a region of interest (dashed white box). Bottom: illustration of the different strain fields at 10% axial strain.

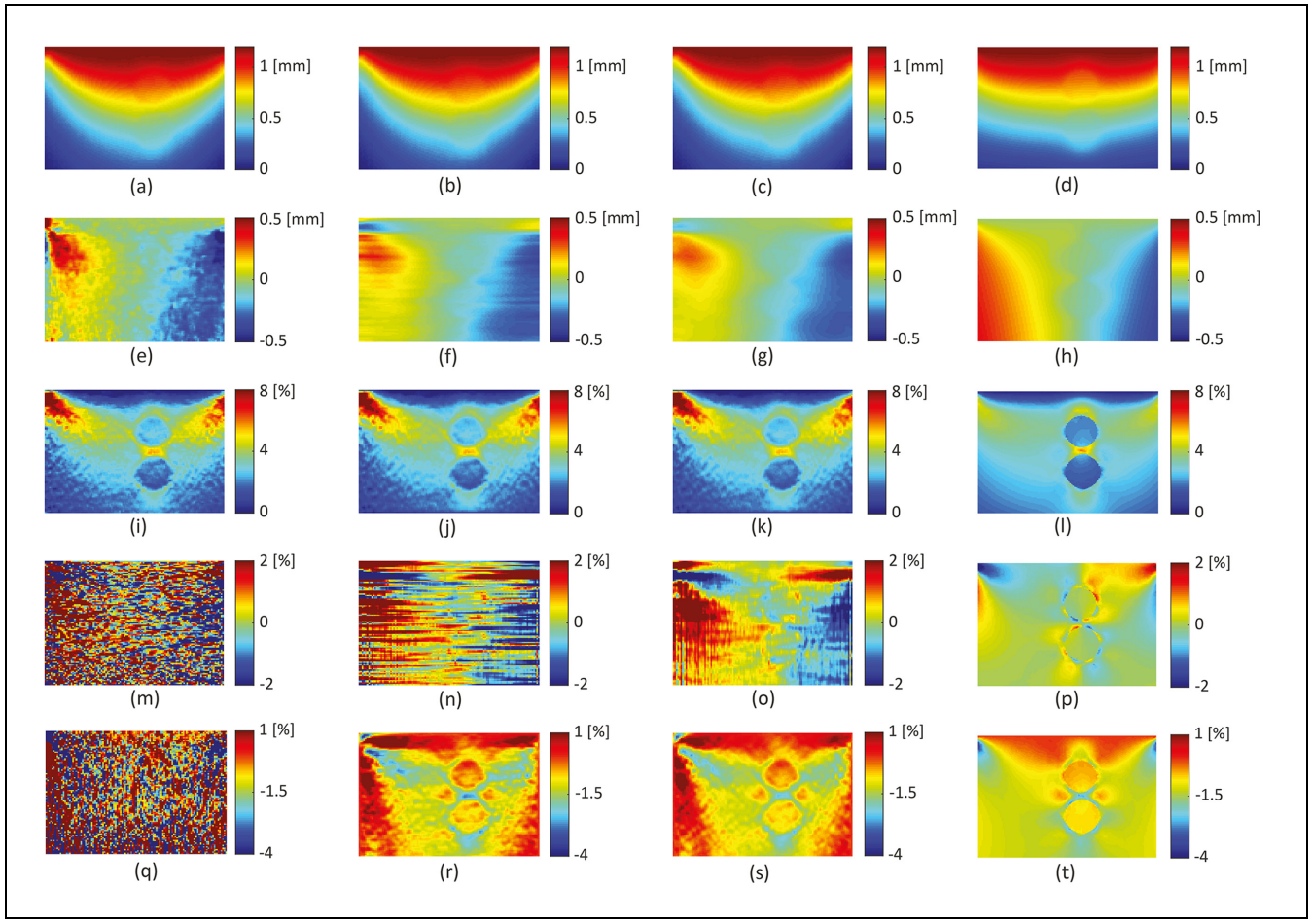

Figure 6. Phantom results - case #2. From top to bottom: (a-d) axial displacement, (e-h) lateral displacement, (i-l) axial strain, (m-p) shear strain, (q-t) and lateral strain. From left to right: fields before regularization, after regularization without penalty terms ($\beta_1 = \beta_2 = 0$), after regularization with $\beta_1 = \beta_2 = 0.05$, and fields resulting from the modeling of the experiment with *Comsol Multiphysics*®.

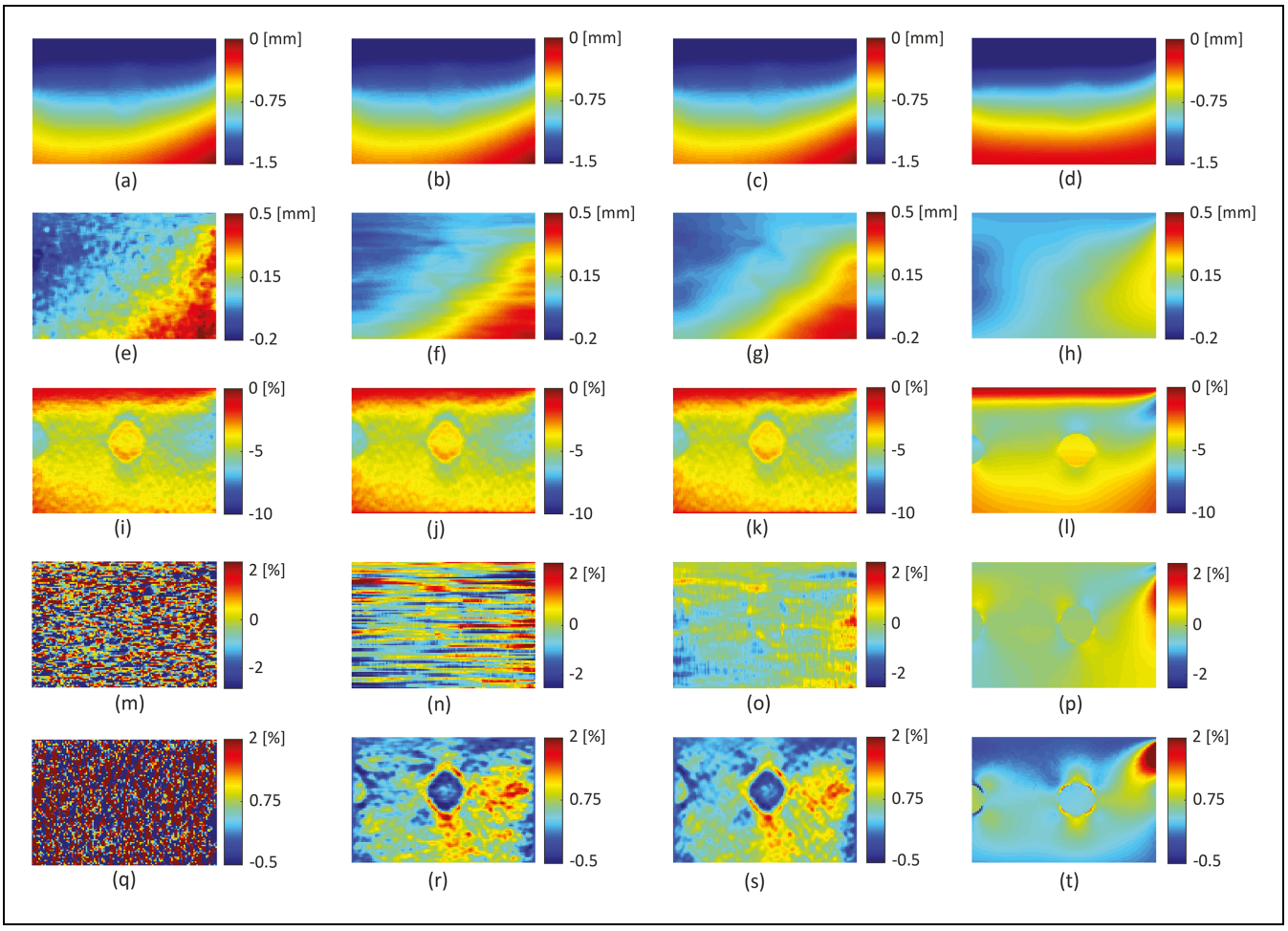

Figure 7. Phantom results - case #3. From top to bottom: (a-d) axial displacement, (e-h) lateral displacement, (i-l) axial strain, (m-p) shear strain, and (q-t) lateral strain. From left to right: fields before regularization, after regularization without penalty terms ($\beta_1 = \beta_2 = 0$), after regularization with $\beta_1 = \beta_2 = 0.05$, and fields resulting from the modeling of the experiment with *Comsol Multiphysics*®.

strain. Compared with the simulation (Figures 6 and 7, (p)), the field presents line artifacts along the lateral direction that corrupt the shear strain patterns. This effect of "horizontal lines" can also be noted in the lateral displacement (Figures 6 and 7, (f)), but they are much more attenuated. The regularization without penalty terms significantly improved the lateral strain field, and the inclusions are easily detectable in both regularized axial and lateral strain images (Figures 6 and 7, (j) and (r)).

After regularization, but this time with $\beta_1 = \beta_2 = 0.05$, the axial displacement (Figures 6 and 7, (c)) and strain (Figures 6 and 7, (k)) remain visually unchanged, as expected, and the lateral displacement (Figures 6 and 7, (g)) becomes smoother compared with (Figures 6 and 7, (e)–(f)). Yet, this smoothing does not affect the lateral strain (Figures 6 and 7, (s)), which is similar to the field regularized with $\beta_1 = \beta_2 = 0$ (Figures 6 and 7, (r)). Nevertheless, adding the penalty terms greatly improves the shear strain images, making the presence of the inclusions more easily detectable (Figures 6 and 7, (o)). Above all, the shear patterns show now similarities with those from the simulations (Figures 6 and 7, (p)).

These visual observations are supported by the computed CNR values (Table 1). More precisely, $CNR_{lateral}$ significantly improve with the regularization, with values in the range of [0.54–9.57] for $\beta_1 = \beta_2 = 0.05$ and [0.68–9.40] for $\beta_1 = \beta_2 = 0$ versus [0.09–0.38] before regularization. We can note that relatively similar values of CNR are obtained whether or not the penalty terms are used. Moreover, in both cases, $CNR_{lateral}$ values after regularization are quite close to CNR_{axial} ones, which confirms the fact that the inclusions are now as easily detectable in the lateral strain images as they are in the axial ones. A specific comment can be made for the bottom inclusion in case #2, which shows more variations in the results than the other cases. For this inclusion, the

Table 1. Contrast-to-Noise Ratios (CNRs) Before and After Regularization, and the Corresponding Multiplying Factors (MFs) Obtained for the Phantom Cases.[a]

	CNR_{axial}			$CNR_{lateral}$		
	Before	After	MF	Before	After	MF
Case #1—right	9.38	10.07	1.07	0.36	9.40	26.47
	9.38	10.33	1.10	0.36	9.57	26.95
Case #1—left	10.51	11.19	1.06	0.35	8.83	24.93
	10.51	11.51	1.09	0.35	8.63	24.36
Case #2—top right	7.57	7.89	1.04	0.27	5.54	20.32
	7.57	8.23	1.09	0.27	6.88	25.26
Case #2—top left	7.10	7.82	1.10	0.38	5.84	15.33
	7.10	8.04	1.13	0.38	6.32	16.59
Case #2—bottom right	2.20	2.30	1.05	0.31	0.68	2.16
	2.20	2.36	1.07	0.31	0.54	1.72
Case #2—bottom left	3.76	3.98	1.06	0.09	3.25	34.86
	3.76	4.12	1.10	0.09	3.68	39.49
Case #3—right	5.90	6.44	1.09	0.14	5.57	38.62
	5.90	6.62	1.12	0.14	6.80	47.12
Case #3—left	3.82	4.14	1.08	0.10	2.97	29.73
	3.82	4.27	1.12	0.10	3.72	37.25

For case #2, CNR values are provided for each of the two inclusions. Lines in gray correspond to regularization performed with $\beta_1 = \beta_2 = 0.05$ while for the others $\beta_1 = \beta_2 = 0$.

[a]For each of the three phantom cases considered, CNRs and MFs are calculated by selecting the background region on the right (as illustrated in Figure 2(a)) or on the left (Figure 2(b)) of the inclusion.

MF is extremely different, 2.16 and 34.86 ($\beta_1 = \beta_2 = 0$) or 1.72 and 39.49 ($\beta_1 = \beta_2 = 0.05$), depending on where the background region is selected. This difference is due to the higher heterogeneity in the strain values for the region selected on the right of the inclusion. Concerning the axial strain, we showed that the regularization process has no visible impact on the field whatever the value of β_1 or β_2. Overall, a slight improvement in CNR_{axial} can be observed, with an MF ranging from 1.04 to 1.10 ($\beta_1 = \beta_2 = 0$) and from 1.07 to 1.13 ($\beta_1 = \beta_2 = 0.05$).

In Vivo Results

The results obtained with breast tissues are presented here. Once again, the regularization effect on the axial displacement (Figures 8–10, (a)–(c) and strain (Figures 8–10, (g)–(i) remains limited, while it drastically improves the lateral components (Figures 8–10, (d)–(f), and Figures 8–10, (m)–(o)). In both axial and lateral regularized strain fields, the abnormal areas are perfectly distinguishable and deform less than the surrounding tissues, which is in agreement with the observations generally made in elastography studies.[53,54] The introduction of the penalty terms ($\beta_1 = \beta_2 = 0.05$) allows us to obtain shear strain fields (Figures 8–10, (l)) that are much less noisy, while preserving the regularized axial (Figures 8–10, (i)) and lateral (Figures 8–10, (o)) strain images. This last observation is supported by the similar values of CNR between fields regularized with $\beta_1 = \beta_2 = 0$ and $\beta_1 = \beta_2 = 0.05$ (Table 2). Overall, we can observe an increase in the $CNR_{lateral}$, with values in the range of [1.98–6.50] versus [0.08–0.34] without regularization. Just like with phantoms, the CNR_{axial} values obtained for the in vivo experiments are slightly enhanced after regularization, with an MF ranging from 1.04 to 1.34. Further analysis is nonetheless difficult, due to the high complexity of biological media and the lack of information regarding the mechanical properties of the examined tissues, which also prevent any simulations from being performed. It should however be added that a coherent evolution of the displacement and strain fields with compression was observed for all in vivo cases, as it was also for the phantoms. An illustration is provided with the invasive ductal carcinoma—case #5 (Figure 11).

Discussion

In the present study, we investigated the feasibility of estimating the 2D strain tensor of biological tissues in quasi-static ultrasound elastography. The proposed approach includes a regularization method, which enforces the (quasi-) incompressibility property of soft tissues and penalizes strong variations within the displacement fields. Such variations are nearly absent from the axial displacement, because this field is already accurately estimated by our motion-tracking technique and smooth. Moreover, simulation results obtained with a linear elastic, isotropic, and homogeneous medium subjected to 10 different

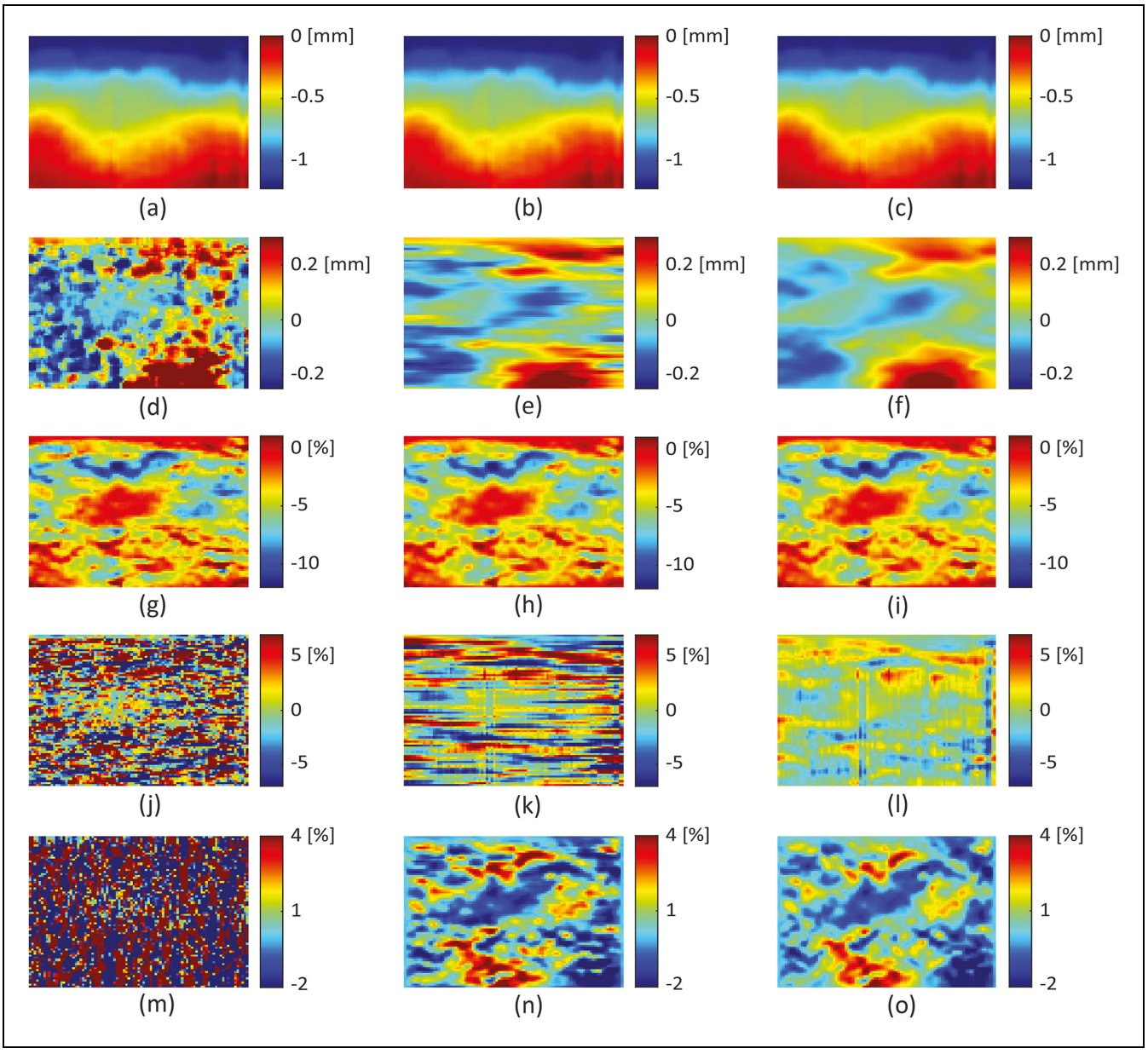

Figure 8. In vivo results - case #4. From top to bottom: (a-c) axial displacement, (d-f) lateral displacement, (g-i) axial strain, (j-l) shear strain, and (m-o) lateral strain. From left to right: fields before regularization, after regularization without penalty terms ($\beta_1 = \beta_2 = 0$), and after regularization with $\beta_1 = \beta_2 = 0.05$.

levels of compression have also shown that the axial strain images before regularization have mean values that are already very close to the actual ones with very low standard deviations (Figure 5). This explains the choice made for the regularization method to have a very limited impact on the axial displacement, whereas significant modifications in the lateral displacement are allowed and expected. This has led to the selection of specific weighting coefficients (λ_1, λ_2, β_1, and β_2), which were kept unchanged for all of the cases examined. Nevertheless, in future work, if additional tests reveal the need of parameter adjustment to the data, an automatic selection of these parameters will be considered. Although the regularized axial fields display no visible modifications compared with the initial ones, a slight increase in the CNR_{axial} values was noted. Moreover, the inclusions/lesions become as clearly visible in lateral strain images as they are in the axial ones, which was not the case before regularization. These results are quantitatively supported by the significant increase in the $CNR_{lateral}$ values, both for phantoms (Table 1) and in vivo tissues (Table 2). Finally, for the phantom cases, modeling of the

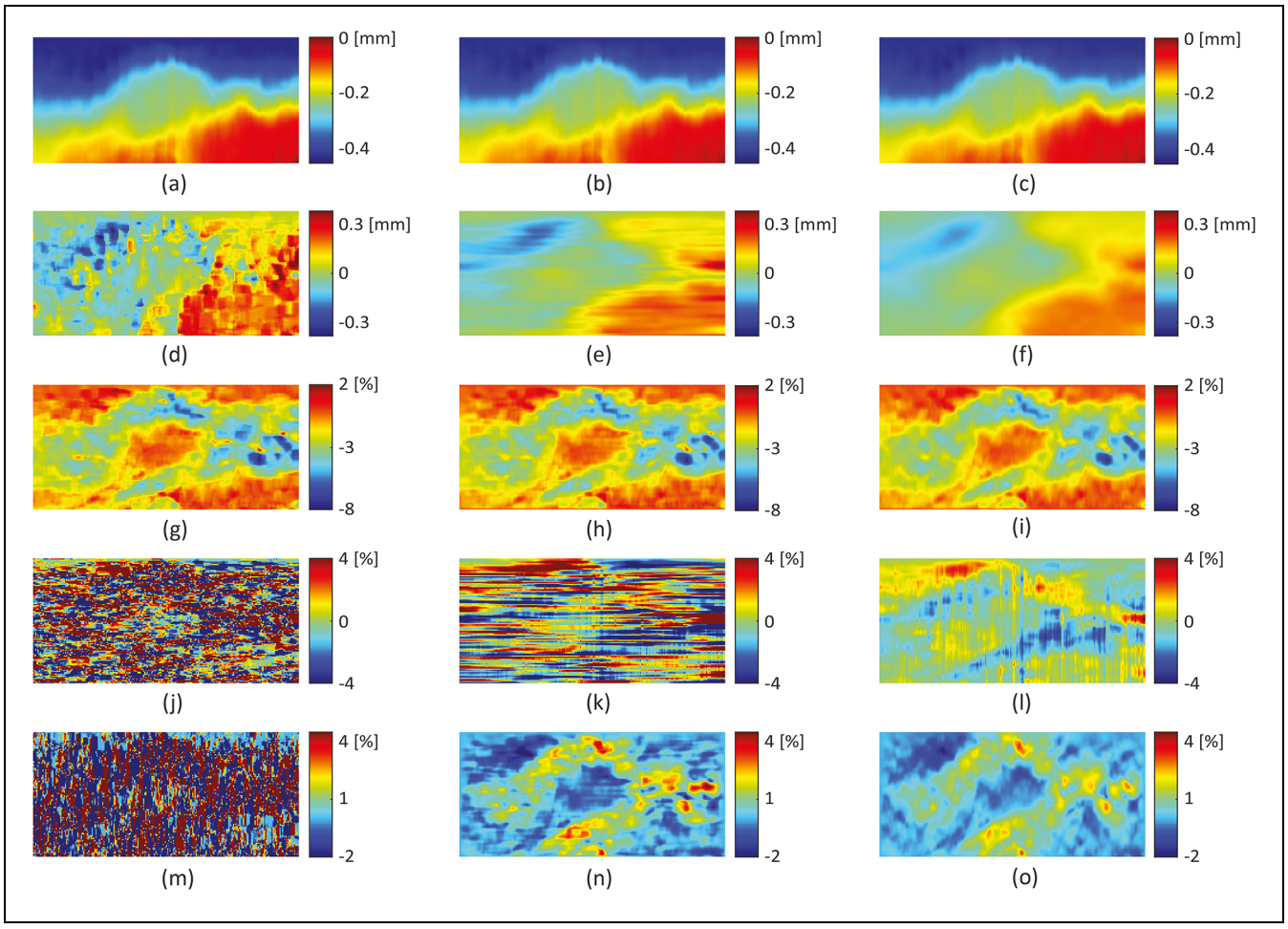

Figure 9. In vivo results - case #5. From top to bottom: (a-c) axial displacement, (d-f) lateral displacement, (g-i) axial strain, (j-l) shear strain, and (m-o) lateral strain. From left to right: fields before regularization, after regularization without penalty terms ($\beta_1 = \beta_2 = 0$), and after regularization with $\beta_1 = \beta_2 = 0.05$.

experiments were also performed, and similarities in terms of strain patterns and values were observed between experimental and simulated fields (Figures 6 and 7).

Concerning the accuracy of the regularized fields, one limitation can, however, be raised from the uniaxial compression test (Figure 5). Indeed, the lateral strain values along the vertical edges of the images are much lower than those expected, while the rest of the image is more accurately estimated (see values of the mean strains and standard deviations within the selected region of interest, Figure 5). This loss of accuracy can be explained by the boundary conditions chosen. Indeed, these conditions are used to compute the spatial derivatives at the borders, and they may be responsible for erroneous estimates if insufficiently adapted. In such a case, the areas affected will be more extended than only the vertical edges, since the regularization method employed is an iterative method. However, except for these border regions, results were found to be close to the theoretical values. This tends to indicate that, for experimental data to be used with this method, it is preferable to acquire them with the region of interest positioned in the middle of the image, along the lateral direction. This, actually, corresponds to the current practice in ultrasound imaging.

Guo et al.[41], who used only the incompressibility property (i.e., $\beta_1 = \beta_2 = 0$ in Figures 6–10), also reported an improvement in the lateral strain images. Concerning the shear strain, these images were not presented. However, as shown in the present study, some "horizontal lines" can be observed in the lateral displacement when regularization is performed using the incompressibility condition alone with the data fidelity terms, and these lines are particularly reinforced in the shear strain because this field requires the differentiation of the lateral displacement along the axial direction. Introducing penalty terms allows us to obtain smoother lateral displacement fields

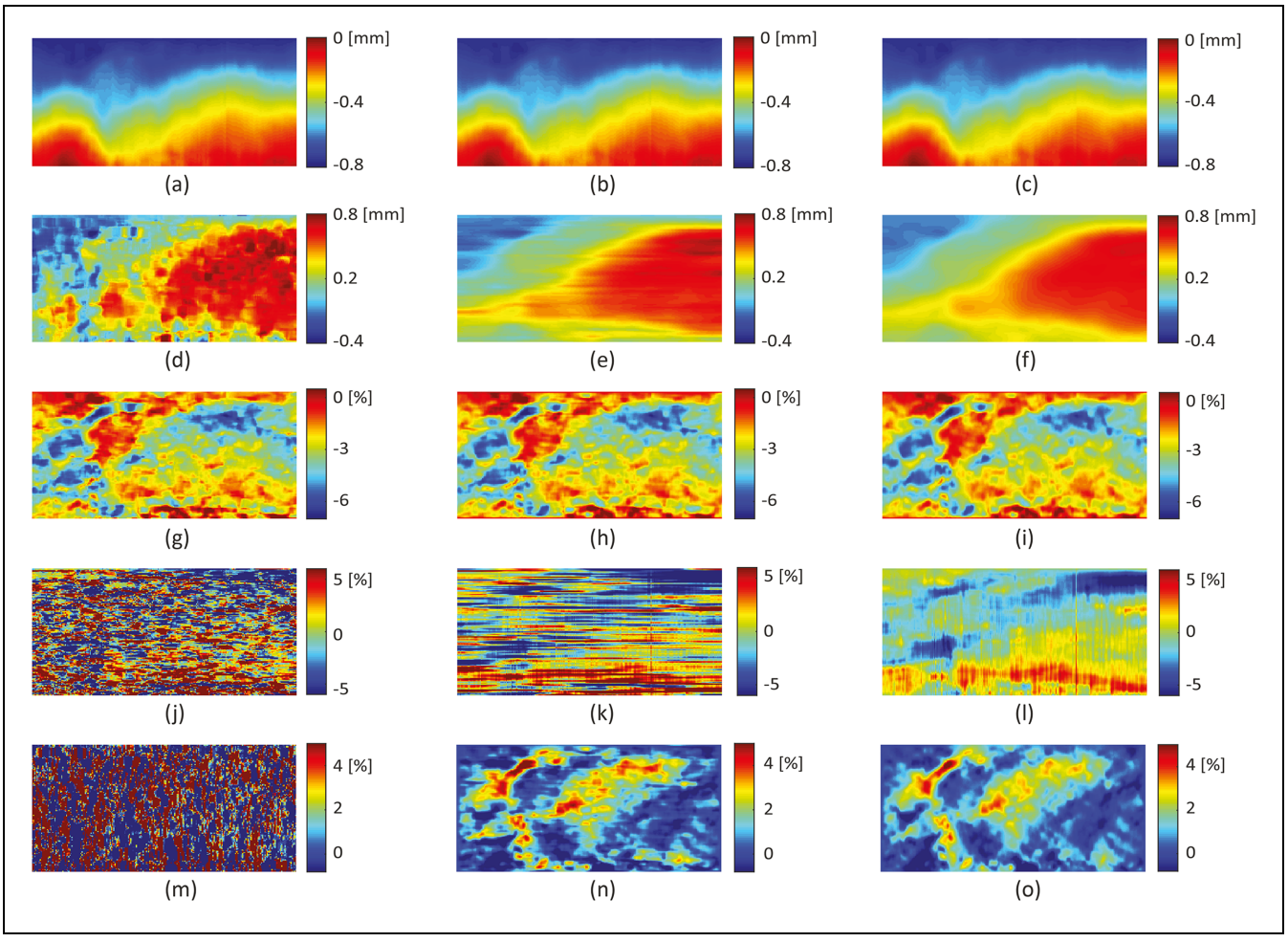

Figure 10. In vivo results - case #6. From top to bottom: (a-c) axial displacement, (d-f) lateral displacement, (g-i) axial strain, (j-l) shear strain, and (m-o) lateral strain. From left to right: fields before regularization, after regularization without penalty terms ($\beta_1 = \beta_2 = 0$), and after regularization with $\beta_1 = \beta_2 = 0.05$.

Table 2. Contrast-to-Noise Ratios (CNRs) Before and After Regularization, and the Corresponding Multiplying Factors (MFs) Obtained for the Breast Tissues.[a]

	CNR_{axial}			$CNR_{lateral}$		
	Before	After	MF	Before	After	MF
Case #4—right	7.38	8.00	1.08	0.15	4.76	31.82
	7.38	8.28	1.12	0.15	5.39	36.05
Case #4—left	4.60	4.80	1.04	0.22	2.16	9.95
	4.60	4.92	1.07	0.22	2.36	10.90
Case #5—right	3.82	4.41	1.16	0.16	1.98	12.18
	3.82	5.09	1.34	0.16	2.52	15.51
Case #5—left	5.74	6.26	1.09	0.08	3.46	42.66
	5.74	6.74	1.17	0.08	3.66	45.06
Case #6—right	4.38	4.59	1.05	0.27	5.65	20.61
	4.38	4.99	1.14	0.27	6.50	23.68
Case #6—left	4.13	4.41	1.07	0.34	4.48	13.30
	4.13	4.81	1.16	0.34	4.57	13.58

Lines in gray correspond to regularization performed with $\beta_1 = \beta_2 = 0.05$ while for the others $\beta_1 = \beta_2 = 0$.
[a]For each of the three in vivo cases considered, CNRs and MFs are calculated by selecting the background region on the right (Figure 2(a)) or on the left (Figure 2(b)) of the lesion.

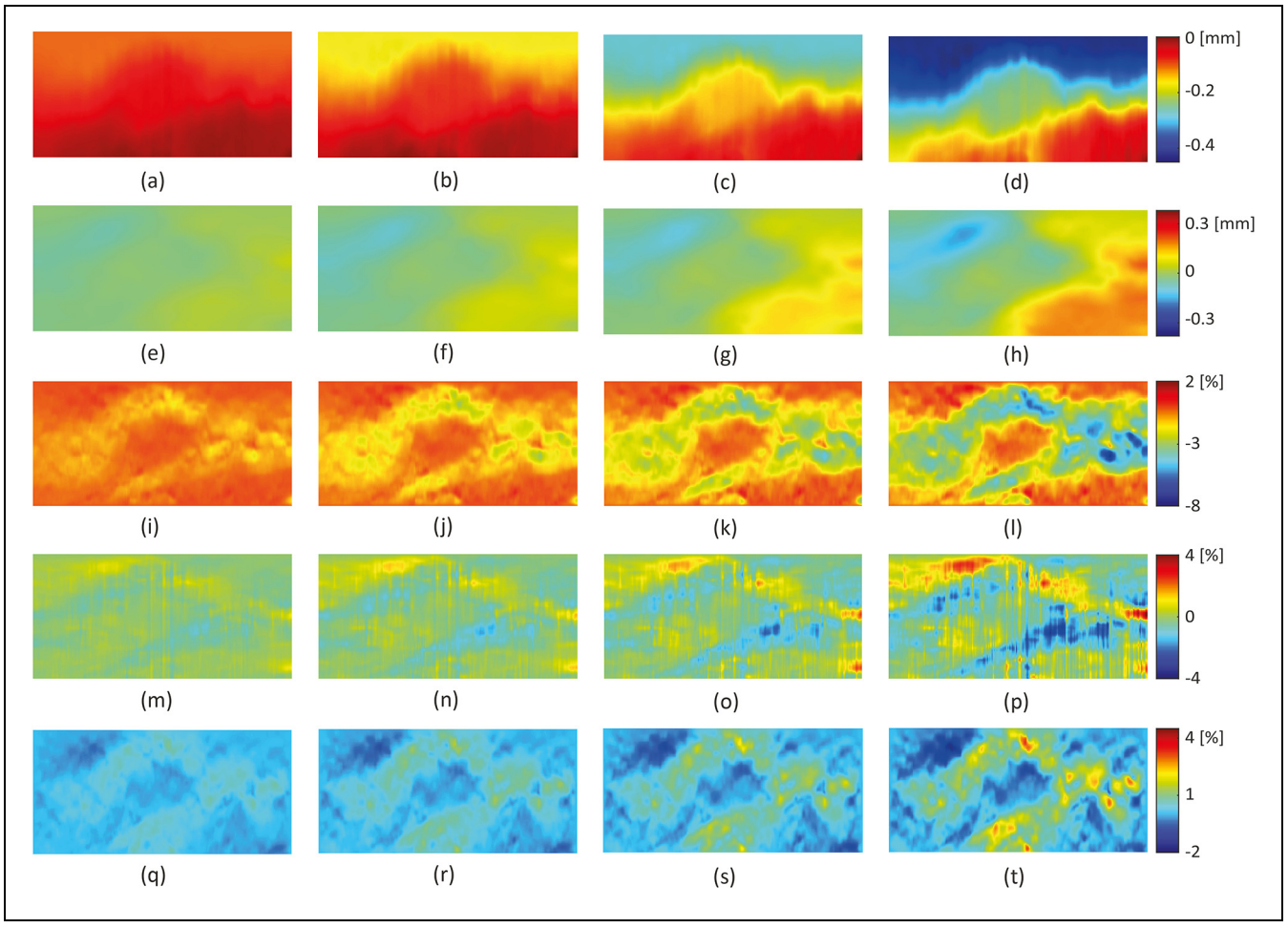

Figure 11. Illustration of fields evolution over time with in vivo tissues - case #5. From left to right: displacement and strain images during tissue compression. From top to bottom: (a-d) axial displacement, (e-h) lateral displacement, (i-l) axial strain, (m-p) shear strain, and (q-t) lateral strain. In Figure 12, parts 12a-12i are labeled but those parts should also be included in the figure legends. Please edit the legend to include those parts.

and to remove these line artifacts. As a consequence, regularized shear strain images are less noisy, and the shear patterns become more visible. For the phantom cases, the regularized shear strain images, and more particularly their patterns, are in agreement with the simulations.

In addition to shear strain maps, other types of images can be obtained with our method, such as rotation elastograms, defined as:

$$\omega_{xy} = \frac{1}{2}\left(\frac{\partial u_y}{\partial x} - \frac{\partial u_x}{\partial y}\right) \tag{5}$$

with, as a reminder, u_y and u_x the axial and lateral displacement, and x and y the lateral and axial spatial variables, respectively. Figure 12 presents the estimated rotation elastograms for each of the cases investigated in this study. As observed for the regularized shear strain, the patterns of rotation are clearly detectable around the inclusions/lesions, and, for the phantom cases (Figure 12(d)–(f)),in agreement with the corresponding simulations (Figure 12(a)–(c)). Concerning the in vivo results, further analysis is obviously difficult as no information about the mechanical properties of the tissues is available. Nevertheless, what should be retained is that any improvement in the 2D strain tensor imaging method will benefit rotation elastography as well.

Currently, two stopping criteria are used in the regularization method, namely, the fact that the change in the displacement fields is lower than a threshold ($C_{rite} < \xi = 10^{-8}$, (3)) and the maximum number of iterations ($N = 50,000$) is reached. Generally, regularization stops because of the first criterion. Figure 13 shows, for phantom case #1 and in vivo case #5, the evolution of C_{rite}, as well as the regularized lateral displacement at four different iterative steps. In case #1, two phases can be observed. First, the regularized lateral displacements display substantial modifications with a smoothing

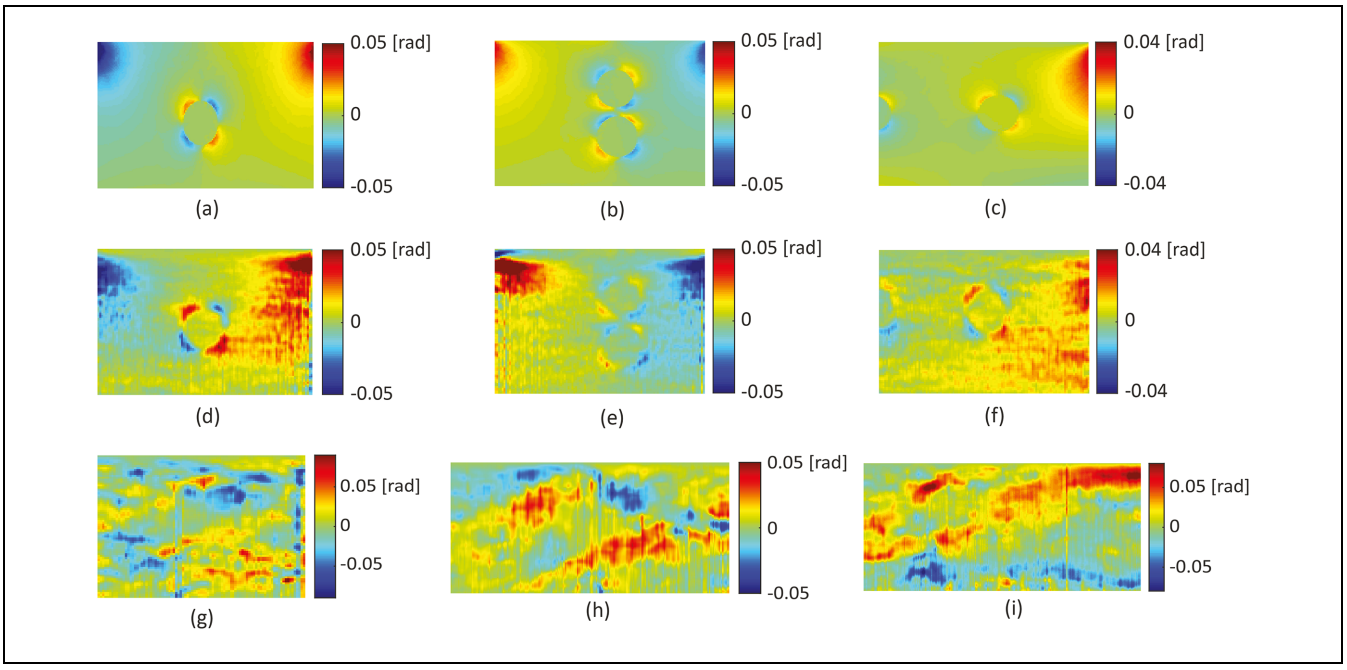

Figure 12. Rotation elastograms from phantom and in vivo cases, after regularization ($\beta_1 = \beta_2 = 0.05$). (a-c) rotation elastograms resulting from the modeling with *Comsol Multiphysics*® of the phantom experiments, cases #1, #2, and #3, (d-f) and corresponding experimental results. (g-i) in vivo breast tissue rotation elastograms from cases #4, #5, and #6.

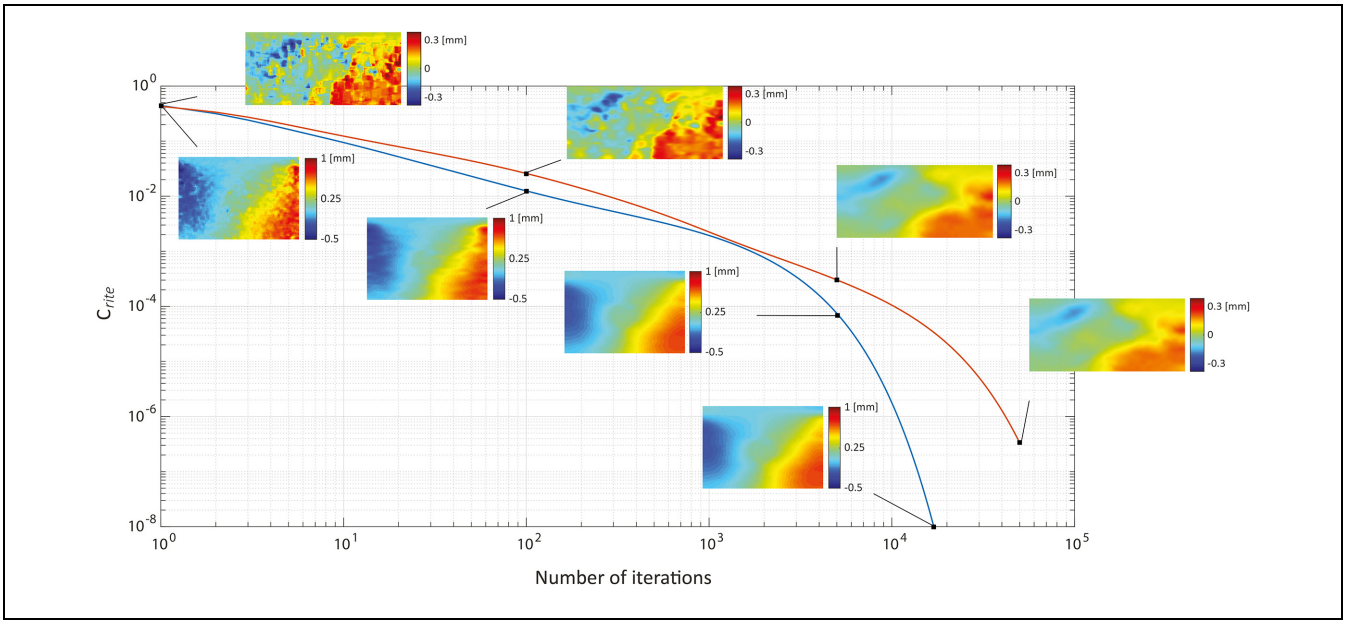

Figure 13. Evolution of C_{rite} during the regularization process for phantom case #1 (blue) and in vivo case #5 (red). The regularized lateral displacement is displayed for four different iteration values.

effect, and then additional iterations produce no visible changes. Interestingly, in case #5, even though the maximum number of iterations is reached, the same observation can be made, that is, the last two lateral displacement fields present no visible modifications, and C_{rite} (Figure 13, red curve) follows an evolution similar to that of case #1 (Figure 13, blue curve). These results suggest that, visible changes in the different fields should no longer occur for this case. Moreover, we can note with the different cases examined in this study, that the

value of the threshold could be less restrictive without losing the contribution of the regularization method, which would also allow to reduce the computation time. The proposed approach could in addition benefit from the introduction of an adaptive step size, instead of using a constant one for all iterations. For this first version of the method, real time aspects were not taken into consideration, but for information, a few seconds on a standard laptop were necessary for fields to be regularized when the 1^{st} stopping criterion was reached.

Finally, it is important to highlight that, although our method is a 2D approach, the regularized strain fields are consistent with media deforming in 3D. It should also be specified that, both the regularization and motion estimation methods can be easily extended to the third dimension to visualize the full strain tensor, which will be part of future developments.

Conclusion

In this study, 2D strain tensor imaging was investigated involving the use of a regularization method, which combines the (quasi-) incompressibility property of soft tissues and penalty terms. Our results show the strong contribution of this method when facing complex and noisy data, especially for the lateral components of displacement and strain. Furthermore, the proposed approach enables us to obtain shear strain images and rotation elastograms. Beyond a more complete analysis of the medium strain, these results are particularly interesting for mechanical parameter reconstruction, which will be the subject of future research work.

Acknowledgments

This study is based on work done at the PILoT facility (PILoT, INSA LYON, Bât. Leonard De Vinci, 21 Av. Jean Capelle 69621 Villeurbanne, France). This work was perfomed within the framework of the LABEX CELYA (ANR-10-LABX-0060/ANR-11-IDEX-0007) and LABEX PRIMES (ANR-11-LABX-0063/ANR-11-IDEX-0007).

Declaration of Conflicting Interests

The author(s) declared no potential conflicts of interest with respect to the research, authorship, and/or publication of this article.

Funding

The author(s) received no financial support for the research, authorship, and/or publication of this article.

ORCID iD

Anne-Lise Duroy https://orcid.org/0000-0003-0567-1383

References

1. Larin KV, Sampson DD. Optical coherence elastography - OCT at work in tissue biomechanics [Invited]. Biomed Opt Express. 2017;8(2):1172-202.
2. Mariappan YK, Glaser KJ, Ehman RL. Magnetic resonance elastography: A review. Clinical Anatomy. 2010; 23(5):497-511.
3. Ophir J, Céspedes I, Ponnekanti H, Yazdi Y, Li X. Elastography: a quantitative method for imaging the elasticity of biological tissues. Ultrason Imaging. 1991;13(2): 111-34.
4. Wells PN, Liang HD. Medical ultrasound: imaging of soft tissue strain and elasticity. J R Soc Interface. 2011;8(64): 1521-49.
5. Krouskop TA, Wheeler TM, Kallel F, Garra BS, Hall T. Elastic moduli of breast and prostate tissues under compression. Ultrason Imaging. 1998;20(4):260-74.
6. Varghese T. Quasi-static ultrasound elastography. Ultrasound Clin. 2009;4(3):323-38.
7. Alhabshi SMI, Rahmat K, Abdul Halim N, Aziz S, Radhika S, Gan GC, et al. Semi-quantitative and qualitative assessment of breast ultrasound elastography in differentiating between malignant and benign lesions. Ultrasound Med Biol. 2013;39(4):568-78.
8. Bojanic K, Katavic N, Smolic M, Peric M, Kralik K, Sikora M, et al. Implementation of elastography score and strain ratio in combination with B-mode ultrasound avoids unnecessary biopsies of breast lesions. Ultrasound Med Biol. 2017;43(4):804-16.
9. Leong LC, Sim LS, Lee YS, Ng FC, Wan CM, Fook-Chong SM, et al. A prospective study to compare the diagnostic performance of breast elastography versus conventional breast ultrasound. Clin Radiol. 2010; 65(11):887-94.
10. Gürüf A, Öztürk M, Bayrak İK, Polat AV. Shear wave versus strain elastography in the differentiation of benign and malignant breast lesions. Turk J Med Sci. 2019;49(5): 1509-17.
11. Kim HJ, Kim SM, Kim B, La Yun B, Jang M, Ko Y, et al. Comparison of strain and shear wave elastography for qualitative and quantitative assessment of breast masses in the same population. Sci Rep. 2018;8:6197.
12. Seo M, Ahn HS, Park SH, Lee JB, Choi BI, Sohn YM, et al. Comparison and combination of strain and shear wave elastography of breast masses for differentiation of benign and malignant lesions by quantitative assessment: Preliminary Study. J Ultrasound Med. 2018;37(1):99-109.
13. Konofagou E, Ophir J. A new elastographic method for estimation and imaging of lateral displacements, lateral strains, corrected axial strains and Poisson's ratios in tissues. Ultrasound Med Biol. 1998;24(8):1183-99.
14. Berry GP, Bamber JC, Miller NR, Barbone PE, Bush NL, Armstrong CG. Towards an acoustic model-based poroelastic imaging method: II. experimental investigation. Ultrasound Med Biol. 2006;32(12):1869-85.
15. Islam MT, Chaudhry A, Tang S, Tasciotti E, Righetti R. A new method for estimating the effective Poisson's ratio in ultrasound poroelastography. IEEE Trans Med Imaging. 2018;37(5):1178-91.

16. Konofagou EE, Harrigan TP, Ophir J, Krouskop TA. Poroelastography: imaging the poroelastic properties of tissues. Ultrasound Med Biol. 2001;27(10):1387-97.
17. Righetti R, Ophir J, Srinivasan S, Krouskop TA. The feasibility of using elastography for imaging the Poisson's ratio in porous media. Ultrasound Med Biol. 2004;30(2): 215-28.
18. Hendriks GAGM, Chen C, Hansen HHG, de Korte CL. 3-D single breath-hold shear strain estimation for improved breast lesion detection and classification in automated volumetric ultrasound scanners. IEEE Trans Ultrason Ferroelectr Freq Control. 2018;65(9):1590-9.
19. Konofagou EE, Harrigan T, Ophir J. Shear strain estimation and lesion mobility assessment in elastography. Ultrasonics. 2000;38(1-8):400-4.
20. Rao M, Varghese T, Madsen EL. Shear strain imaging using shear deformations. Med Phys. 2008;35(2):412-23.
21. Xu H, Varghese T, Madsen EL. Analysis of shear strain imaging for classifying breast masses: Finite element and phantom results. Med Phys. 2011;38(11):6119-27.
22. Kothawala A, Chandramoorthi S, Reddy NRK, Thittai AK. Spatial compounding technique to obtain rotation elastogram: A Feasibility Study. Ultrasound Med Biol. 2017;43(6):1290-301.
23. Lokesh B, Chintada B, Thittai A. Rotation elastogram estimation using synthetic transmit-aperture technique: A feasibility study. Ultrason Imaging. 2017;39(3):189-204.
24. Barbone PE, Oberai AA. Elastic modulus imaging: some exact solutions of the compressible elastography inverse problem. Phys Med Biol. 2007;52(6):1577-93.
25. Doyley MM. Model-based elastography: a survey of approaches to the inverse elasticity problem. Phys Med Biol. 2012;57(3):R35-73.
26. Nitta NN, Shiina TS. A method of tissue elasticity estimation based on three-dimensional displacement vector. Jpn J Appl Phys. 2000;39:3225-9.
27. Maurice RL, Ohayon J, Frétigny Y, Bertrand M, Soulez G, Cloutier G. Noninvasive Vascular Elastography: Theoretical Framework. IEEE Trans Med Imaging. 2004;23(2): 164-80.
28. Brusseau E, Kybic J, Deprez JF, Basset O. 2-D locally regularized tissue strain estimation from radio-frequency ultrasound images: theoretical developments and results on experimental data. IEEE Trans Med Imaging. 2008;27(2):145-60.
29. Deprez JF, Brusseau E, Schmitt C, Cloutier G, Basset O. 3D estimation of soft biological tissue deformation from radio-frequency ultrasound volume acquisitions. Med Image Anal. 2009;13(1):116-27.
30. Liu K, Zhang P, Shao J, Zhu X, Zhang Y, Bai J. A 2D strain estimator with numerical optimization method for soft-tissue elastography. Ultrasonics. 2009;49(8):723-32.
31. Lopata RGP, Nillesen MM, Hansen HHG, Gerrits IH, Thijssen JM, de Korte CL. Performance Evaluation of methods for Two-Dimensional displacement and strain estimation using ultrasound radio frequency data. Ultrasound Med Biol. 2009;35(5):796-812.
32. Jiang J, Hall TJ. A coupled subsample displacement estimation method for ultrasound-based strain elastography. Phys Med Biol. 2015;60(21):8347-64.
33. Pan X, Liu K, Shao J, Gao J, Huang L, Bai J, et al. Performance comparison of rigid and affine models for motion estimation using ultrasound radio-frequency signals. IEEE Trans Ultrason Ferroelectr Freq Control. 2015;62(11): 1928-43.
34. Peng B, Xian Y, Zhang Q, Jiang J. Neural-network-based motion tracking for breast ultrasound strain elastography: an initial assessment of performance and feasibility. Ultrason Imaging. 2020;42(2):74-91.
35. Techavipoo U, Chen Q, Varghese T, Zagzebski JA. Estimation of displacement vectors and strain tensors in elastography using angular insonifications. IEEE Trans Med Imaging. 2004;23(12):1479-89.
36. Xu H, Varghese T. Normal and shear strain imaging using 2D deformation tracking on beam steered linear array datasets. Med Phys. 2013;40(1):012902.
37. Selladurai S, Thittai AK. Actuator-assisted subpitch translation-capable transducer for elastography: Preliminary Performance Assessment. Ultrason Imaging. 2020;42(1):15-26.
38. Jensen JA, Munk P. A new method for estimation of velocity vectors. IEEE Trans Ultrason Ferroelectr Freq Control. 1998;45(3):837-51.
39. Liebgott H, Fromageau J, Wilhjelm JE, Vray D, Delachartre P. Direct estimation of the lateral strain field using a double oscillating point spread function with a scaling factor estimator. Proc. of SPIE Medical Imaging. 2004;5373: 163-72.
40. Babaniyi OA, Oberai AA, Barbone PE. Recovering vector displacement estimates in quasistatic elastography using sparse relaxation of the momentum equation. Inverse Probl Sci Eng. 2017;25(3):326-62.
41. Guo L, Xu Y, Xu Z, Jiang J. A PDE-based regularization algorithm toward reducing speckle tracking noise: a feasibility study for ultrasound breast elastography. Ultrason Imaging. 2015;37(4):277-93.
42. Hu Z, Zhang H, Yuan J, Lu M, Chen S, Liu H. An $H\infty$ strategy for strain estimation in ultrasound elastography using biomechanical modeling constraint. PLoS One. 2013;8(9):e73093.
43. Al Mukaddim R, Meshram NH, Varghese T. Locally optimized correlation-guided Bayesian adaptive regularization for ultrasound strain imaging. Phys Med Biol. 2020;65(6): 065008.
44. Rivaz H, Boctor EM, Choti MA, Hager GD. Real-time regularized ultrasound elastography. IEEE Trans Med Imaging. 2011;30(4):928-45.
45. Lubinski M, Emelianov S, Raghavan K, Yagle A, Skovoroda A, O'Donnell M. Lateral displacement estimation using tissue incompressibility. IEEE Trans Ultrason Ferroelectr Freq Control. 1996;43(2):247-56.
46. Richards MS, Barbone PE, Oberai AA. Quantitative three-dimensional elasticity imaging from quasi-static deformation: a phantom study. Phys Med Biol. 2009;54(3):757-79.
47. Skovoroda AR, Lubinski MA, Emelianov SY, O'Donnell M. Nonlinear estimation of the lateral displacement using tissue incompressibility. IEEE Trans Ultrason Ferroelectr Freq Control. 1998;45(2):491-503.

48. Duroy AL, Detti V, Coulon A, Basset O, Brusseau E. 2D tissue strain tensor imaging in quasi-static ultrasound elastography. In: IEEE engineering in medicine and biology society. 2021
49. Brusseau E, Detti V, Coulon A, Maissiat E, Boublay N, Berthezène Y, et al. In vivo response to compression of 35 breast lesions observed with a Two-Dimensional locally regularized strain estimation method. Ultrasound Med Biol. 2014;40(2):300-12.
50. Alam SK, Ophir J, Konofagou EE. An adaptive strain estimator for elastography. IEEE Trans Ultrason Ferroelectr Freq Control. 1998;45(2):461-72.
51. Brusseau E, Perrey C, Delachartre P, Vogt M, Vray D, Ermert H. Axial strain imaging using a local estimation of the scaling factor from RF ultrasound signals. Ultrason Imaging. 2000;22(2):95-107.
52. Srinivasan S, Kallel F, Souchon R, Ophir J. Analysis of an adaptive strain estimation technique in elastography. Ultrason Imaging. 2002;24(2):109-18.
53. Hall TJ, Zhu Y, Spalding CS. In vivo real-time freehand palpation imaging. Ultrasound Med Biol. 2003;29(3):427-35.
54. Ozsoy A, Acar D, Barca AN, Aktas H, Araz L, Ozkaraoglu O, et al. Diagnostic performance of real-time strain sonoelastography in BI-RADS 4 and 5 breast masses. Diagn Interven Imaging. 2016;97(9):883-9.